

FULLY COUPLED SIMULATION OF COSMIC REIONIZATION. III. STOCHASTIC EARLY REIONIZATION BY THE SMALLEST GALAXIES

PENGFEI CHEN¹, MICHAEL L. NORMAN^{1,2}, HAO XU², AND JOHN H. WISE³

¹CASS, University of California, San Diego, 9500 Gilman Drive, La Jolla, CA 92093; pec008@ucsd.edu, mlnorman@ucsd.edu

²San Diego Supercomputer Center, 9500 Gilman Drive, La Jolla, CA 92093; hxu@ucsd.edu and

³Center for Relativistic Astrophysics, School of Physics, Georgia Institute of Technology, 837 State Street, Atlanta, GA 30332; jwise@gatech.edu

Draft version May 2, 2022

ABSTRACT

Previously we identified a new class of early galaxy that we estimate contributes up to 30% of the ionizing photons responsible for reionization. These are low mass halos in the range $M_{\text{halo}} = 10^{6.5} - 10^8 M_{\odot}$ that have been chemically enriched by supernova ejecta from prior Pop III star formation. Despite their low star formation rates, these Metal Cooling halos (MCs) are significant sources of ionizing radiation, especially at the onset of reionization, due to their high number density and ionizing escape fractions. Here we present a fully-coupled radiation hydrodynamic simulation of reionization that includes these MCs as well the more massive hydrogen atomic line cooling halos. Our method is novel: we perform halo finding inline with the radiation hydrodynamical simulation, and assign escaping ionizing fluxes to halos using a probability distribution function (PDF) measured from the galaxy-resolving *Renaissance Simulations*. The PDF captures the mass dependence of the ionizing escape fraction as well as the probability that a halo is actively forming stars. With MCs, reionization starts earlier than if only halos of $10^8 M_{\odot}$ and above are included, however the redshift when reionization completes is only marginally affected as this is driven by more massive galaxies. Because star formation is intermittent in MCs, the earliest phase of reionization exhibits a stochastic nature, with small HII regions forming and recombining. Only later, once halos of mass $\sim 10^9 M_{\odot}$ and above begin to dominate the ionizing emissivity, does reionization proceed smoothly in the usual manner deduced from previous studies. This occurs at $z \approx 10$ in our simulation.

Keywords: galaxies: formation – galaxies: high-redshift – methods: numerical — radiative transfer

1. INTRODUCTION

The relative contributions to reionization from halos in different mass ranges are still not clear. A useful taxonomy for discussion we follow here was introduced by [Iliev et al. \(2007\)](#). The halos hosting early galaxies could be divided into three categories according to their mass. The first are minihalos (MHs, $M_{\text{halo}} < 10^8 M_{\odot}$), which host the formation of Population III stars but otherwise are not thought to be efficient star formers due to their low virial temperatures and low H_2 cooling efficiency. The second are low-mass atomic-cooling halos (LMACHs, $10^8 M_{\odot} < M_{\text{halo}} < 10^9 M_{\odot}$), which have virial temperatures just above the threshold to excite H atomic line cooling and form stars inefficiently. The third are high-mass atomic cooling halos (HMACHs, $M_{\text{halo}} > 10^9 M_{\odot}$), which cool and form stars more efficiently than the LMACHs.

Some work has been done to study the role of LMACHs and MHs in reionization ([Iliev et al. 2007](#); [Choudhury et al. 2008](#); [Shapiro et al. 2012](#); [Iliev et al. 2012](#); [Ahn et al. 2012](#); [Wyithe & Loeb 2013](#)) which show that with the smallest galaxies included reionization begins earlier and the intergalactic electron-scattering optical depth τ_{es} is boosted. However these authors find the late phase of reionization is still dominated by HMACHs and the overlap redshift z_{ov} is not significantly affected. In these studies the galaxy properties are not simulated directly, but rather assumed using simple parameterized models which directly relate a halo’s mass to its ionizing emissivity. For the smallest galaxies this relation is exceedingly uncertain due to a variety of complex physical processes. For example, the formation of the smallest galaxies is possibly suppressed due to the large Lyman-Werner background which photodissociates the primary coolant H_2 ([Ahn](#)

[et al. 2012](#)), and due to supernova feedback which depletes the halo of gas ([Wyithe & Loeb 2013](#)). Some simulations are used to predict the signatures of reionization on the high redshift 21cm background, and to discuss how 21cm observations could help to distinguish the relative contributions of galaxies of different masses to reionization ([Shapiro et al. 2012](#); [Iliev et al. 2012](#)).

However, recently [Wise et al. \(2014\)](#) have shown using AMR radiation hydrodynamic simulations that minihalos which have been chemically enriched by supernova ejecta from prior Pop III star formation can cool and form stars, and moreover significantly contribute to the overall ionizing photon budget of reionization. We refer to this new class of halos as metal-line cooling halos, or MCs. Follow-on simulations (the *Renaissance Simulations*) in much larger volumes by [Xu et al. \(2016b\)](#) provide the star formation rates (SFR), intermittency, and ionizing escape fractions in the MCs, LMACHs, and HMACHs with extremely high resolution and good statistics. Using these results as our input, we revisit the problem: what is the role of the lowest mass halos in the reionization process? The main improvement of our work compared with previous work is that the simulations shown here are fully coupled cosmological radiation hydrodynamic simulations, with a time-dependent treatment of the ionization kinetics, and emissivities assigned to the source halos dynamically, considering the intermittency of the contribution from MCs.

We find that because star formation is intermittent in MCs, the earliest phases of reionization exhibits a stochastic nature, with small HII regions forming and recombining. Only later, after the characteristic halo mass scale has reached $\sim 10^9 M_{\odot}$, does reionization proceed smoothly in the usual manner de-

duced from earlier studies. With no adjustable model parameters and only using the galaxy properties from the Renaissance Simulations, our 1152³ simulation in a 14.4 comoving Mpc box begins reionizing at $z = 20$, is 10% ionized at $z = 10$, and fully ionizes at $z = 7.3$. Although our box is not large enough to be statistically representative, our simulation is marginally consistent with the latest measurement of the electron scattering optical depth to the CMB suggesting that the chemical contribution of Pop III stars may be more important than their ionizing contribution.

This paper is organized as follows. We summarize the relevant results from Xu et al. (2016b) in Section 2. The description of computational method and inputs to the simulations is provided in Section 3. We show results in Section 4 and offer discussion and conclusions in Section 5.

2. IONIZING PHOTONS FROM THE SMALLEST GALAXIES

Unlike the previous papers in this series (So et al. 2014; Norman et al. 2015), where ionizing emissivities were calculated from a simple star formation/feedback recipe incorporated in the simulation itself, here we import results from much higher resolution simulations which calculate the escaping ionizing photons of high redshift galaxies directly. How this is done is described in Secs. 3.2 and 3.3. This approach enormously relaxes the spatial resolution requirement on the global reionization simulation and takes advantage of more precise simulation results. Uniform grids may be employed for the reionization simulation, however they must have sufficient mass and spatial resolution to accurately capture the halo population of importance. In addition, we are able to use moment methods for the radiation transport, which do not get bogged down as reionization completes as some ray tracing methods do (Norman et al. 2015).

We import the results of Xu et al. (2016b) who performed three high-resolution AMR simulations of regions of different over-densities in order to study the abundance, environmental dependence, and escape fraction f_{esc} of the smallest galaxies during reionization. The so-called *Renaissance Simulations* (see also O’Shea et al. (2015)) include both Pop II and Pop III star formation and their radiative, mechanical, and chemical feedback. They find that for $M_{halo} \lesssim 10^7 M_\odot$, the mean f_{esc} is between about 0.4 to 0.6, then f_{esc} declines smoothly over the mass range $10^7 M_\odot < M_{halo} < 10^8 M_\odot$ to less than 0.05 for LMACHs ($10^8 M_\odot < M_{halo} < 10^9 M_\odot$), then rises to about 0.1 to 0.2 for HMACHs ($M_{halo} > 10^9 M_\odot$) (cf. Figs. 15-17 in Xu et al. 2016b). They also calculate the fraction of halos with active star formation as a function of M_{halo} , and find that the fraction is less than 0.1 for $\sim 10^7 M_\odot$ halos, ~ 0.5 for $\sim 10^8 M_\odot$ halos and then 1.0 for halos larger than $10^{8.5} M_\odot$ (cf. Fig 19 in Xu et al. 2016b). With those results they derive the number of escaped ionizing photons per second $\dot{N}_{ion,esc}$ as a function of M_{halo} . For smaller halos ($10^7 M_\odot < M_{halo} < 10^9 M_\odot$), the MCs and LMACHs, there is a large scatter in the gas fraction, the star formation efficiency, the escape fraction f_{esc} and thus $\dot{N}_{ion,esc}$. So rather than try to fit this data the $\dot{N}_{ion,esc} - M_{halo}$ relation is reproduced as a table (Table 1, not published in Xu et al. (2016b)). The table shows the probability distribution of $\dot{N}_{ion,esc}$ in different M_{halo} bins.

For HMACHs, the correlation is tighter and they derive a fit of this relation,

$$\log_{10}(\dot{N}_{ion,esc}) = 36.033 + 1.675 \times \log_{10}(M_{halo}), \quad (1)$$

which we adopt here. Both Table 1 and Equation 1 are derived from their simulation of a normal-density region at redshift 12.5. Since they find that the galaxy properties are principally dependent on their mass, and are almost independent on their forming environment and redshift, we take the $\dot{N}_{ion,esc} - M_{halo}$ relation (Table 1 and Equation 1) as the input for our simulations during the whole reionization era.

3. NUMERICAL METHODOLOGY

3.1. Basic Model

All simulations presented in this paper are carried out with the publicly available Enzo code (Bryan et al. 2014). Enzo solves the Eulerian equations of cosmological radiation hydrodynamics using the Particle-Mesh method for the dark matter with CIC interpolation (Hockney & Eastwood 1988), a dual-energy formulation of the Piecewise Parabolic Method for the gas (Bryan et al. 1995), and FFTs for the gravitational field. We use it in its 6-species primordial gas chemistry mode, wherein the nonequilibrium evolution of H, H⁺, He, He⁺, He⁺⁺ and e⁻ is computed using the backward difference formula (BDF) solver of Anninos et al. (1997). We use Enzo’s built-in implicit flux-limited diffusion (FLD) radiative transfer solver (Reynolds et al. 2009; Norman et al. 2015) for the transfer of ionizing photons, which are treated in the grey approximation. In Norman et al. (2015) we show that Enzo’s FLD and Moray ray tracing radiative transfer solver (Wise & Abel 2011) give nearly identical ionization histories in a reionization test problem. We use FLD because it is much faster, especially as the volume becomes fully ionized. The ionizing sources are assumed to be low metallicity star forming galaxies in halos of mass $M_{halo} \geq 10^7 M_\odot$. Thus we ignore the radiative contribution of Pop III stars. We return to the impact of this assumption in the discussion section. The spectral energy distribution (SED) of the stellar radiation is the same as in So et al. (2014), which is the SED derived by Ricotti et al. (2002) for a $Z = 0.04 Z_\odot$ stellar population but truncated above 4 Ryd. We also include in the simulation star formation and supernova feedback using the simple parameterized model of So et al. (2014), however we do not use it for calculating radiative feedback because of the improved, halo-based, resolution-insensitive model introduced here. Because we input into the simulation the number of escaping ionizing photons measured at the virial radius from the *Renaissance Simulations* (Sec. 2), we do not need to assume an ionizing escape fraction. Therefore f_{esc} is not a parameter of the simulation. We also only need to resolve the virial radii of the halos of importance, which greatly relaxes the spatial resolution requirement, but not the mass resolution (see below). A WMAP7 Λ CDM cosmological model is used: $\Omega_M = 0.27$, $\Omega_\Lambda = 0.73$, $\Omega_b = 0.047$, $h = 0.7$, $\sigma_8 = 0.82$, and $n = 0.95$, where the parameters have the usual definitions. All simulations start from redshift 99 and run until the simulation volume is fully ionized.

In this paper we present three simulations differing only in mass and spatial resolution and box size. All use inline halo finding and assign emissivities to halos as described in Secs. 3.2 and 3.3. Their properties are summarized in Table 2. The first two constitute a resolution study, which show the importance of including halos as small as $10^7 M_\odot$. 256_all is a 256³ cell/particle simulation in a 6.4 comoving Mpc box. This is

Table 1
 M_{halo} dependent escaped ionizing photons rate $\dot{N}_{\text{ion,esc}}$ used in all simulations in Table 2.

	10 ^{7.0}	10 ^{7.1}	10 ^{7.2}	10 ^{7.3}	10 ^{7.4}	10 ^{7.5}	10 ^{7.6}	10 ^{7.7}	10 ^{7.8}	10 ^{7.9}
0.00	0.00	0.00	0.00	0.00	0.00	0.00	0.00	0.00	0.00	0.00
...
0.76	0.00	0.00	0.00	0.00	0.00	0.00	0.00	0.00	0.00	0.00
0.78	0.00	0.00	0.00	0.00	0.00	0.00	0.00	0.00	0.00	1.20 × 10 ⁴⁶
0.80	0.00	0.00	0.00	0.00	0.00	0.00	0.00	0.00	0.00	3.08 × 10 ⁴⁸
0.82	0.00	0.00	0.00	0.00	0.00	0.00	0.00	0.00	9.60 × 10 ⁴⁷	3.37 × 10 ⁴⁸
0.84	0.00	0.00	0.00	0.00	0.00	0.00	0.00	0.00	3.67 × 10 ⁴⁸	5.19 × 10 ⁴⁸
0.86	0.00	0.00	0.00	0.00	0.00	0.00	0.00	0.00	7.20 × 10 ⁴⁸	2.34 × 10 ⁴⁹
0.88	0.00	0.00	0.00	0.00	0.00	0.00	0.00	1.90 × 10 ⁴⁸	1.56 × 10 ⁴⁹	5.04 × 10 ⁴⁹
0.90	0.00	0.00	0.00	1.44 × 10 ⁴⁸	6.40 × 10 ⁴⁸	1.12 × 10 ⁴⁶	4.42 × 10 ⁴⁶	8.67 × 10 ⁴⁸	1.66 × 10 ⁴⁹	8.86 × 10 ⁴⁹
0.92	0.00	0.00	0.00	1.68 × 10 ⁴⁹	1.44 × 10 ⁴⁹	1.81 × 10 ⁴⁹	1.39 × 10 ⁴⁹	5.68 × 10 ⁴⁹	2.35 × 10 ⁴⁹	1.39 × 10 ⁵⁰
0.94	0.00	0.00	5.50 × 10 ⁴⁸	5.41 × 10 ⁴⁹	5.18 × 10 ⁴⁹	4.11 × 10 ⁴⁹	4.64 × 10 ⁴⁹	9.74 × 10 ⁴⁹	2.87 × 10 ⁴⁹	1.81 × 10 ⁵⁰
0.96	0.00	5.35 × 10 ⁴⁹	3.81 × 10 ⁴⁹	7.95 × 10 ⁴⁹	1.97 × 10 ⁵⁰	7.44 × 10 ⁴⁹	1.12 × 10 ⁵⁰	2.38 × 10 ⁵⁰	1.02 × 10 ⁵⁰	1.88 × 10 ⁵⁰
0.98	1.82 × 10 ⁵⁰	3.35 × 10 ⁵⁰	1.69 × 10 ⁵⁰	2.43 × 10 ⁵¹	5.21 × 10 ⁵⁰	3.49 × 10 ⁵⁰	3.00 × 10 ⁵⁰	3.71 × 10 ⁵⁰	1.67 × 10 ⁵⁰	7.50 × 10 ⁵⁰
	10 ^{8.0}	10 ^{8.1}	10 ^{8.2}	10 ^{8.3}	10 ^{8.4}	10 ^{8.5}	10 ^{8.6}	10 ^{8.7}	10 ^{8.8}	10 ^{8.9}
0.00	0.00	0.00	0.00	0.00	0.00	0.00	9.30 × 10 ⁴⁸	8.15 × 10 ⁴⁹	4.91 × 10 ⁴⁹	1.12 × 10 ⁵⁰
0.02	0.00	0.00	0.00	0.00	0.00	0.00	9.30 × 10 ⁴⁸	8.15 × 10 ⁴⁹	4.91 × 10 ⁴⁹	1.12 × 10 ⁵⁰
0.04	0.00	0.00	0.00	0.00	0.00	0.00	9.30 × 10 ⁴⁸	8.15 × 10 ⁴⁹	4.91 × 10 ⁴⁹	1.12 × 10 ⁵⁰
0.06	0.00	0.00	0.00	0.00	0.00	0.00	9.30 × 10 ⁴⁸	8.15 × 10 ⁴⁹	4.91 × 10 ⁴⁹	1.12 × 10 ⁵⁰
0.08	0.00	0.00	0.00	0.00	0.00	0.00	9.30 × 10 ⁴⁸	8.15 × 10 ⁴⁹	4.91 × 10 ⁴⁹	1.12 × 10 ⁵⁰
0.10	0.00	0.00	0.00	0.00	0.00	0.00	9.30 × 10 ⁴⁸	8.15 × 10 ⁴⁹	4.91 × 10 ⁴⁹	1.12 × 10 ⁵⁰
0.12	0.00	0.00	0.00	0.00	0.00	0.00	9.30 × 10 ⁴⁸	8.15 × 10 ⁴⁹	4.91 × 10 ⁴⁹	1.12 × 10 ⁵⁰
0.14	0.00	0.00	0.00	0.00	0.00	0.00	9.30 × 10 ⁴⁸	8.15 × 10 ⁴⁹	4.91 × 10 ⁴⁹	1.12 × 10 ⁵⁰
0.16	0.00	0.00	0.00	0.00	0.00	0.00	9.30 × 10 ⁴⁸	1.64 × 10 ⁵⁰	4.91 × 10 ⁴⁹	1.12 × 10 ⁵⁰
0.18	0.00	0.00	0.00	0.00	0.00	0.00	9.30 × 10 ⁴⁸	1.64 × 10 ⁵⁰	4.91 × 10 ⁴⁹	1.12 × 10 ⁵⁰
0.20	0.00	0.00	0.00	0.00	1.45 × 10 ⁴⁷	0.00	9.30 × 10 ⁴⁸	1.64 × 10 ⁵⁰	4.91 × 10 ⁴⁹	1.12 × 10 ⁵⁰
0.22	0.00	0.00	0.00	0.00	1.45 × 10 ⁴⁷	0.00	9.30 × 10 ⁴⁸	1.64 × 10 ⁵⁰	4.91 × 10 ⁴⁹	1.12 × 10 ⁵⁰
0.24	0.00	0.00	0.00	0.00	1.45 × 10 ⁴⁷	0.00	9.83 × 10 ⁴⁸	1.64 × 10 ⁵⁰	4.91 × 10 ⁴⁹	1.12 × 10 ⁵⁰
0.26	0.00	0.00	0.00	0.00	1.45 × 10 ⁴⁷	0.00	9.83 × 10 ⁴⁸	1.64 × 10 ⁵⁰	4.91 × 10 ⁴⁹	1.12 × 10 ⁵⁰
0.28	0.00	0.00	0.00	0.00	1.45 × 10 ⁴⁷	0.00	9.83 × 10 ⁴⁸	1.64 × 10 ⁵⁰	4.91 × 10 ⁴⁹	1.12 × 10 ⁵⁰
0.30	0.00	0.00	0.00	0.00	1.45 × 10 ⁴⁷	0.00	9.83 × 10 ⁴⁸	1.64 × 10 ⁵⁰	4.91 × 10 ⁴⁹	1.12 × 10 ⁵⁰
0.32	0.00	0.00	0.00	0.00	1.45 × 10 ⁴⁷	0.00	9.83 × 10 ⁴⁸	3.92 × 10 ⁵⁰	6.88 × 10 ⁵⁰	1.12 × 10 ⁵⁰
0.34	0.00	0.00	0.00	0.00	1.45 × 10 ⁴⁷	0.00	9.83 × 10 ⁴⁸	3.92 × 10 ⁵⁰	6.88 × 10 ⁵⁰	1.12 × 10 ⁵⁰
0.36	0.00	0.00	0.00	0.00	1.45 × 10 ⁴⁷	0.00	9.83 × 10 ⁴⁸	3.92 × 10 ⁵⁰	6.88 × 10 ⁵⁰	1.12 × 10 ⁵⁰
0.38	0.00	0.00	0.00	0.00	1.45 × 10 ⁴⁷	0.00	9.83 × 10 ⁴⁸	3.92 × 10 ⁵⁰	6.88 × 10 ⁵⁰	1.12 × 10 ⁵⁰
0.40	0.00	0.00	0.00	0.00	6.38 × 10 ⁴⁸	0.00	9.83 × 10 ⁴⁸	3.92 × 10 ⁵⁰	6.88 × 10 ⁵⁰	1.12 × 10 ⁵⁰
0.42	0.00	0.00	0.00	0.00	6.38 × 10 ⁴⁸	0.00	9.83 × 10 ⁴⁸	3.92 × 10 ⁵⁰	6.88 × 10 ⁵⁰	1.12 × 10 ⁵⁰
0.44	0.00	0.00	0.00	0.00	6.38 × 10 ⁴⁸	0.00	9.83 × 10 ⁴⁸	3.92 × 10 ⁵⁰	6.88 × 10 ⁵⁰	1.12 × 10 ⁵⁰
0.46	0.00	0.00	0.00	0.00	6.38 × 10 ⁴⁸	0.00	9.83 × 10 ⁴⁸	3.92 × 10 ⁵⁰	6.88 × 10 ⁵⁰	1.12 × 10 ⁵⁰
0.48	0.00	0.00	0.00	0.00	6.38 × 10 ⁴⁸	0.00	9.83 × 10 ⁴⁸	3.92 × 10 ⁵⁰	6.88 × 10 ⁵⁰	1.12 × 10 ⁵⁰
0.50	0.00	0.00	0.00	0.00	6.38 × 10 ⁴⁸	0.00	1.16 × 10 ⁴⁹	5.39 × 10 ⁵⁰	6.88 × 10 ⁵⁰	1.54 × 10 ⁵¹
0.52	0.00	0.00	0.00	0.00	6.38 × 10 ⁴⁸	0.00	1.16 × 10 ⁴⁹	5.39 × 10 ⁵⁰	6.88 × 10 ⁵⁰	1.54 × 10 ⁵¹
0.54	0.00	0.00	0.00	0.00	6.38 × 10 ⁴⁸	0.00	1.16 × 10 ⁴⁹	5.39 × 10 ⁵⁰	6.88 × 10 ⁵⁰	1.54 × 10 ⁵¹
0.56	0.00	0.00	0.00	0.00	6.38 × 10 ⁴⁸	1.43 × 10 ⁴⁸	1.16 × 10 ⁴⁹	5.39 × 10 ⁵⁰	6.88 × 10 ⁵⁰	1.54 × 10 ⁵¹
0.58	0.00	0.00	0.00	1.39 × 10 ⁴⁷	6.38 × 10 ⁴⁸	1.43 × 10 ⁴⁸	1.16 × 10 ⁴⁹	5.39 × 10 ⁵⁰	6.88 × 10 ⁵⁰	1.54 × 10 ⁵¹
0.60	0.00	0.00	2.60 × 10 ⁴⁷	1.39 × 10 ⁴⁷	9.03 × 10 ⁴⁹	1.43 × 10 ⁴⁸	1.16 × 10 ⁴⁹	5.39 × 10 ⁵⁰	6.88 × 10 ⁵⁰	1.54 × 10 ⁵¹
0.62	0.00	0.00	2.60 × 10 ⁴⁷	1.39 × 10 ⁴⁷	9.03 × 10 ⁴⁹	1.43 × 10 ⁴⁸	1.16 × 10 ⁴⁹	5.39 × 10 ⁵⁰	6.88 × 10 ⁵⁰	1.54 × 10 ⁵¹
0.64	0.00	2.22 × 10 ⁴⁷	9.04 × 10 ⁴⁷	1.60 × 10 ⁴⁸	9.03 × 10 ⁴⁹	1.43 × 10 ⁴⁸	1.16 × 10 ⁴⁹	5.39 × 10 ⁵⁰	6.88 × 10 ⁵⁰	1.54 × 10 ⁵¹
0.66	0.00	2.22 × 10 ⁴⁷	9.04 × 10 ⁴⁷	1.60 × 10 ⁴⁸	9.03 × 10 ⁴⁹	1.43 × 10 ⁴⁸	1.16 × 10 ⁴⁹	1.12 × 10 ⁵¹	6.96 × 10 ⁵⁰	1.54 × 10 ⁵¹
0.68	0.00	2.22 × 10 ⁴⁷	9.04 × 10 ⁴⁷	1.60 × 10 ⁴⁸	9.03 × 10 ⁴⁹	1.43 × 10 ⁴⁸	1.16 × 10 ⁴⁹	1.12 × 10 ⁵¹	6.96 × 10 ⁵⁰	1.54 × 10 ⁵¹
0.70	0.00	3.08 × 10 ⁴⁸	1.57 × 10 ⁴⁸	8.42 × 10 ⁴⁸	9.03 × 10 ⁴⁹	2.08 × 10 ⁵⁰	1.16 × 10 ⁴⁹	1.12 × 10 ⁵¹	6.96 × 10 ⁵⁰	1.54 × 10 ⁵¹
0.72	0.00	3.08 × 10 ⁴⁸	1.57 × 10 ⁴⁸	8.42 × 10 ⁴⁸	9.03 × 10 ⁴⁹	2.08 × 10 ⁵⁰	1.16 × 10 ⁴⁹	1.12 × 10 ⁵¹	6.96 × 10 ⁵⁰	1.54 × 10 ⁵¹
0.74	0.00	5.77 × 10 ⁴⁸	5.15 × 10 ⁴⁸	8.42 × 10 ⁴⁸	9.03 × 10 ⁴⁹	2.08 × 10 ⁵⁰	5.88 × 10 ⁵⁰	1.12 × 10 ⁵¹	6.96 × 10 ⁵⁰	1.54 × 10 ⁵¹
0.76	0.00	5.77 × 10 ⁴⁸	5.15 × 10 ⁴⁸	1.54 × 10 ⁴⁹	9.03 × 10 ⁴⁹	2.08 × 10 ⁵⁰	5.88 × 10 ⁵⁰	1.12 × 10 ⁵¹	6.96 × 10 ⁵⁰	1.54 × 10 ⁵¹
0.78	3.72 × 10 ⁴⁷	5.77 × 10 ⁴⁸	5.15 × 10 ⁴⁸	1.54 × 10 ⁴⁹	9.03 × 10 ⁴⁹	2.08 × 10 ⁵⁰	5.88 × 10 ⁵⁰	1.12 × 10 ⁵¹	6.96 × 10 ⁵⁰	1.54 × 10 ⁵¹
0.80	2.06 × 10 ⁴⁸	1.53 × 10 ⁴⁹	7.22 × 10 ⁴⁸	1.54 × 10 ⁴⁹	3.78 × 10 ⁵⁰	2.08 × 10 ⁵⁰	5.88 × 10 ⁵⁰	1.12 × 10 ⁵¹	6.96 × 10 ⁵⁰	1.54 × 10 ⁵¹
0.82	2.06 × 10 ⁴⁸	1.53 × 10 ⁴⁹	7.22 × 10 ⁴⁸	4.17 × 10 ⁴⁹	3.78 × 10 ⁵⁰	2.08 × 10 ⁵⁰	5.88 × 10 ⁵⁰	1.25 × 10 ⁵¹	6.96 × 10 ⁵⁰	1.54 × 10 ⁵¹
0.84	1.31 × 10 ⁴⁹	4.39 × 10 ⁴⁹	4.03 × 10 ⁴⁹	4.17 × 10 ⁴⁹	3.78 × 10 ⁵⁰	3.87 × 10 ⁵⁰	5.88 × 10 ⁵⁰	1.25 × 10 ⁵¹	6.96 × 10 ⁵⁰	1.54 × 10 ⁵¹
0.86	1.48 × 10 ⁴⁹	4.39 × 10 ⁴⁹	4.03 × 10 ⁴⁹	4.17 × 10 ⁴⁹	3.78 × 10 ⁵⁰	3.87 × 10 ⁵⁰	5.88 × 10 ⁵⁰	1.25 × 10 ⁵¹	6.96 × 10 ⁵⁰	1.54 × 10 ⁵¹
0.88	1.48 × 10 ⁴⁹	4.39 × 10 ⁴⁹	4.03 × 10 ⁴⁹	1.78 × 10 ⁵⁰	3.78 × 10 ⁵⁰	3.87 × 10 ⁵⁰	5.88 × 10 ⁵⁰	1.25 × 10 ⁵¹	6.96 × 10 ⁵⁰	1.54 × 10 ⁵¹
0.90	1.75 × 10 ⁴⁹	1.60 × 10 ⁵⁰	1.37 × 10 ⁵⁰	1.78 × 10 ⁵⁰	3.78 × 10 ⁵⁰	3.87 × 10 ⁵⁰	5.88 × 10 ⁵⁰	1.25 × 10 ⁵¹	6.96 × 10 ⁵⁰	1.54 × 10 ⁵¹
0.92	3.07 × 10 ⁴⁹	1.60 × 10 ⁵⁰	1.37 × 10 ⁵⁰	1.78 × 10 ⁵⁰	3.78 × 10 ⁵⁰	3.87 × 10 ⁵⁰	5.88 × 10 ⁵⁰	1.25 × 10 ⁵¹	6.96 × 10 ⁵⁰	1.54 × 10 ⁵¹
0.94	3.07 × 10 ⁴⁹	2.62 × 10 ⁵⁰	1.81 × 10 ⁵⁰	2.68 × 10 ⁵⁰	3.78 × 10 ⁵⁰	3.87 × 10 ⁵⁰	5.88 × 10 ⁵⁰	1.25 × 10 ⁵¹	6.96 × 10 ⁵⁰	1.54 × 10 ⁵¹
0.96	7.87 × 10 ⁴⁹	2.62 × 10 ⁵⁰	1.81 × 10 ⁵⁰	2.68 × 10 ⁵⁰	3.78 × 10 ⁵⁰	3.87 × 10 ⁵⁰	5.88 × 10 ⁵⁰	1.25 × 10 ⁵¹	6.96 × 10 ⁵⁰	1.54 × 10 ⁵¹
0.98	7.87 × 10 ⁴⁹	2.62 × 10 ⁵⁰	1.81 × 10 ⁵⁰	2.68 × 10 ⁵⁰	3.78 × 10 ⁵⁰	3.87 × 10 ⁵⁰	5.88 × 10 ⁵⁰	1.25 × 10 ⁵¹	6.96 × 10 ⁵⁰	1.54 × 10 ⁵¹

Notes. M_{halo} is in the unit of $[M_{\odot}]$, while $\dot{N}_{\text{ion,esc}}$ is in the unit of $[\text{s}^{-1}]$.

the same as the test problem presented in [So et al. \(2014\)](#) and [Norman et al. \(2015\)](#), and has the same mass and spatial resolution as the science run analyzed in [So et al. \(2014\)](#). In that case the dark matter particle mass was chosen so that the halo mass function was complete above $M_{\text{halo}} = 10^8 M_{\odot}$. 512_all is a 512^3 cell/particle simulation in the same box. It has 2 times the spatial resolution and 8 times the mass resolution as the 256_all simulation. The halo mass function is complete to $\sim 10^7 M_{\odot}$, essential for including the MCs. These simulations are discussed in Sec. 4.1. The third, 1152_all simulation, is our science run. It is a 1152^3 cell/particle simulation in a 14.4 comoving Mpc box. It has the same mass and spatial resolution as 512_all simulation except in a box 2.25 as large (11.4 times the volume). This simulation is discussed in Sec. 4.2.

3.2. Inline Halo Finding

The Enzo code has an embedded Python capability which allows the user to execute Python scripts which operate on Enzo's internal data structures as the code runs. As the `yt` toolkit ([Turk et al. 2011](#)) is implemented in Python, many of `yt`'s analysis capabilities can be run inline with the computation. This includes the Parallel HOP halo finder ([Skory et al. 2010](#)), which we employ here. In all simulations in Table 2, we use embedded Python to call a script every 20 million years to do the following: (i) find halos and calculate their integral properties, including their virial masses; (ii) assign an emissivity to each halo according to its mass (Section 3.3), (iii) zero the old emissivity field array, and use the halos' positions and emissivities to compute a new emissivity field array (Section 3.3). We choose 20 million years since that is the typical lifetime of OB stars in a coeval stellar population. The emissivity fields are then kept constant until the next inline Python script is called 20 million years later. After clearing all the old emissivity fields, we distribute the new halo emissivity evenly into 27 adjacent cells (a $3 \times 3 \times 3$ cube) centered at the cell that contains the halo's center of mass. Since $\dot{N}_{\text{ion,esc}}$ (Equation 1 and Table 2) already include escaping fractions, by distributing the emissivity field in a larger region instead of the center cell we avoid the ionizing photons being absorbed again.

Because low mass halos ($10^7 M_{\odot} < M_{\text{halo}} < 10^{8.5} M_{\odot}$) do not have a unit probability of actively forming stars ([Xu et al. \(2016b\)](#), Table 1), halos emitting during this 20 million years will likely not emit for the next 20 million years. This is consistent with the results of [Kimm & Cen \(2014\)](#), who find bursty star formation with a duty cycle of about 20 Myr in their simulations of EoR galaxies. In this way we take the intermittency of the contribution from low mass halos into consideration.

3.3. Assigning the Emissivity Field

Instead of using a constant mass-to-light ratio ([Iliev et al. 2007](#)), we assign emissivities to halos according to the $\dot{N}_{\text{ion,esc}} - M_{\text{halo}}$ relations from [Xu et al. \(2016b\)](#). In all simulations, for the larger LMACH halos ($M_{\text{halo}} > 10^9 M_{\odot}$), we use Equation 1 to get their $\dot{N}_{\text{ion,esc}}$. For each halo with mass between 10^7 to $10^9 M_{\odot}$, we generate a random number between 0 and 1 and use it to choose the corresponding $\dot{N}_{\text{ion,esc}}$ from Table 1 in its mass bin. Then we calculate the emissivity of that halo assuming that each ionizing photon has an energy of 21.6eV. Note that the majority of the cells in Table 1 with mass below $10^{8.4} M_{\odot}$ have zero emissivity. For example, for

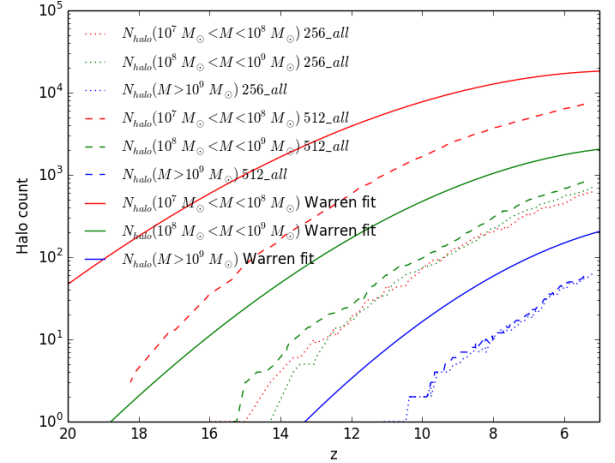


Figure 1. Halo counts vs. redshift in the entire volume for the 256_all and 512_all resolution study simulations for three mass bins: $10^7 \leq M_{\text{halo}}/M_{\odot} \leq 10^8$; $10^8 \leq M_{\text{halo}}/M_{\odot} \leq 10^9$; and $M_{\text{halo}}/M_{\odot} > 10^9$. Note the virtual absence of halos in the lowest mass bin corresponding to metal-line cooling halos (MCs) in the lower resolution simulation 256_all. Warren fits to the halo counts in mass bins are plotted as solid lines.

halos with mass around $10^7 M_{\odot}$, there are only less than 2% of them with nonzero emissivity. This is due to the inefficiency of star formation and the supernova feedback in low mass halos ([Wyithe & Loeb 2013](#)). Each halo larger than $10^{8.6} M_{\odot}$ has nonzero emissivity, but the value may change every 20 million years when a new value is chosen in its mass bin or when it falls into another mass bin.

4. RESULTS

4.1. Resolution study – 256³ and 512³ simulations

To understand the role of the smallest galaxies in reionization we performed two simulations, 256_all and 512_all, both with 6.4 comoving Mpc per side. As described above, the 512_all simulation has twice the spatial resolution and eight times the mass resolution as the 256_all simulation. These two simulations thus constitute a small resolution study. The parameters were chosen so that the halo mass functions are complete to $10^8 M_{\odot}$ and $10^7 M_{\odot}$, respectively.

Figure 1 shows the halo counts in 3 mass bins in both simulations: MCs - $10^7 \leq M_{\text{halo}}/M_{\odot} \leq 10^8$; LMACHs - $10^8 \leq M_{\text{halo}}/M_{\odot} \leq 10^9$; and HMACHs - $M_{\text{halo}}/M_{\odot} > 10^9$. Referring to the 512_all curves, we see MCs, LMACHs, and HMACHs begin forming at $z \sim 18, 15, 11$, respectively. Comparing these curves to their 256_all counterparts, we see that the LMACH and HMACH formation histories are converged, but the MCs are severely underestimated. Due to the higher mass resolution, the MC halo counts in 512_all are 1.5 to 2 orders more than those in 256_all, and they begin forming sooner. The first halo with $M_{\text{halo}} > 10^7 M_{\odot}$ appears at redshift ~ 18.2 in 512_all, which is earlier than redshift ~ 16.0 in 256_all.

Figure 2 shows the evolution of the ionizing photons emitted per comoving cubic Mpc as a function of redshift in the 256_all and 512_all simulations. In the top panel we show the comoving ionizing luminosity density from halos below and above $M_{\text{halo}} = 10^9 M_{\odot}$, as well as the total; in the bottom panel we show the fraction of the total ionizing luminosity coming from halos below $M_{\text{halo}} = 10^9 M_{\odot}$. Looking at the top panel we can see that the HMACH contribution becomes

Table 2
Summary of simulations

Simulation	L_{box} (Mpc)	$N_{\text{cell}} = N_p$	$m_p (M_\odot)$	$100m_p (M_\odot)$	$\Delta x (kpc)$	MC halos included	z_{ov}	total τ_{es}	τ_{es} before z_{ov}
256_all	6.4	256^3	4.8×10^5	4.8×10^7	25	N	5.56	0.0477	0.0097
512_all	6.4	512^3	6×10^4	6×10^6	12.5	Y	5.80	0.0523	0.0120
1152_all	14.4	1152^3	6×10^4	6×10^6	12.5	Y	7.08	0.0691	0.0146

Notes. Box size and resolution element are comoving. z_{ov} is overlap redshift; i.e., when 100% of the volume is ionized to above 99.9% ionization fraction.

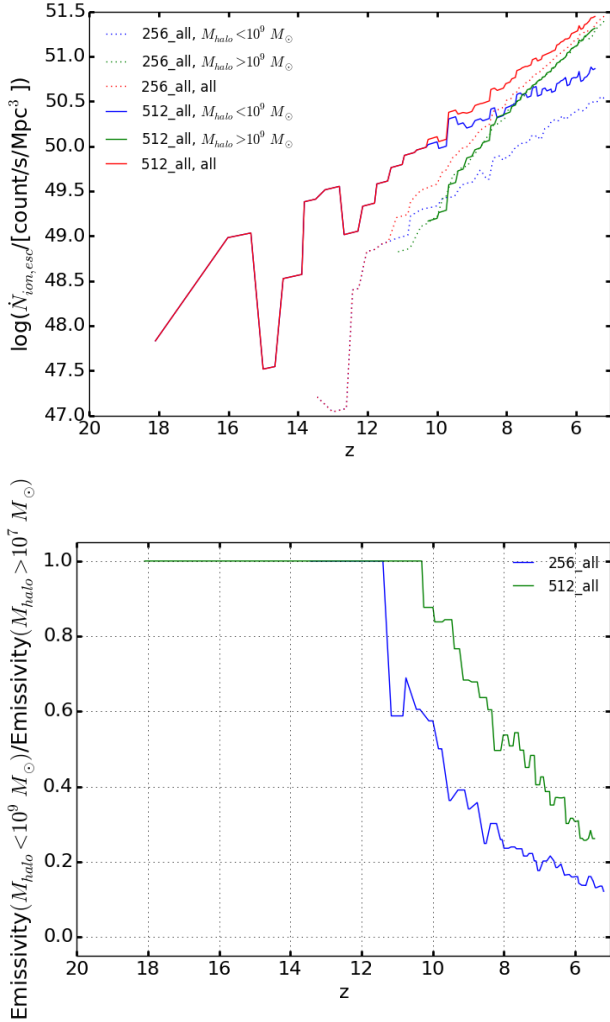


Figure 2. Contribution of halos of different masses to the ionizing emissivity as a function of redshift. Top: comoving ionizing luminosity density vs. redshift from halos below and above $10^9 M_\odot$ and their sum, for the 256_all test simulation (solid lines) and 512_all test simulation (dotted lines). Bottom: Fraction of ionizing photons from halos below $10^9 M_\odot$ versus redshift for 256_all and 512_all. The fraction drops as HMACHs become the dominant ionizing sources.

dominant below $z \sim 10$ in the 256_all simulation, but not until $z \sim 8$ in the 512_all simulation. Because the HMACH population is virtually identical in both simulations, the difference is due to the enhanced contribution of the low mass halos, and specifically the MCs since the LMACH populations are also virtually identical in the two simulations (Fig. 1). Referring to the bottom panel, when there are no HMACHs, all the ionizing photons come from low mass halos so the ratio is one. Then as HMACHs form and become dominant the ratio drops to $\sim 15\%$ (25%) when the reionization completes in

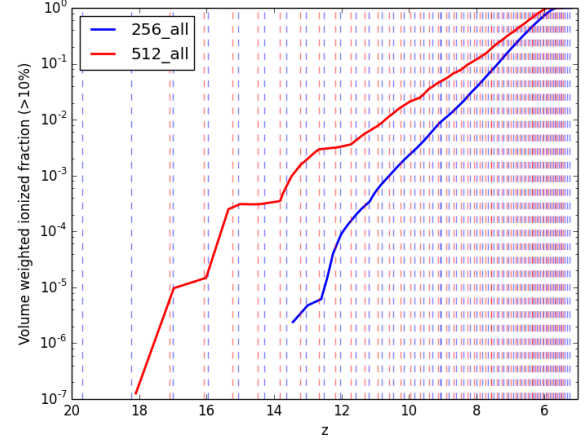


Figure 3. The ionized volume fraction as a function of redshift for 256_all and 512_all. The vertical dashed lines are approximately 20 million years apart indicating the time when inline Python works to find halos and assign ionizing emissivities according to the current halos' mass as described in Sec. 3.3.

256_all(512_all), with some fluctuations in between. The ratio is always higher in 512_all because it has more low mass halos than 256_all but about the same amount of HMACHs.

Figure 3 shows the evolution of the volume fraction ionized above an ionization fraction of 10% for the 256_all and 512_all simulations. The vertical dashed lines indicate when the emissivity field is reset every 20 Myr. Although the first halo with $M_{\text{halo}} > 10^7 M_\odot$ appears at redshift ~ 16.0 in 256_all, the volume doesn't begin to ionize until redshift ~ 13.5 . This is due to the low probability for lower mass halos to emit (Table 1). In 512_all the time between when the first low mass halo emits and when the first HMACH emits is longer than in 256_all, and there are several "stair steps". This is also due to the randomness in the turning on and off of low mass halos. When more halos are turning off, there would be a relatively flat part in the ionized fraction curve. Interestingly, the 512_all simulation completes reionization slightly sooner than the 256_all simulation, this despite the fact that HMACHs have dominated the photon budget by then. This result can be understood as a simple consequence that reionization completion depends on the total number of ionizing photons, which is higher for all redshifts in the 512_all simulation as compared to the 256_all simulation (Fig. 2).

To complete our presentation of the resolution study results, we show in Fig. 4 side-by-side projections of the logarithm of the neutral hydrogen fraction through the 6.4 Mpc volume at $z = 8, 7$ and 6. The color bar is chosen to show highly ionized gas as white, and partially ionized gas as shades of red-brown. The superimposed blue dots is the instantaneous ionizing emissivity field. One can see the larger number of smaller HII regions at earlier redshifts in the higher resolu-

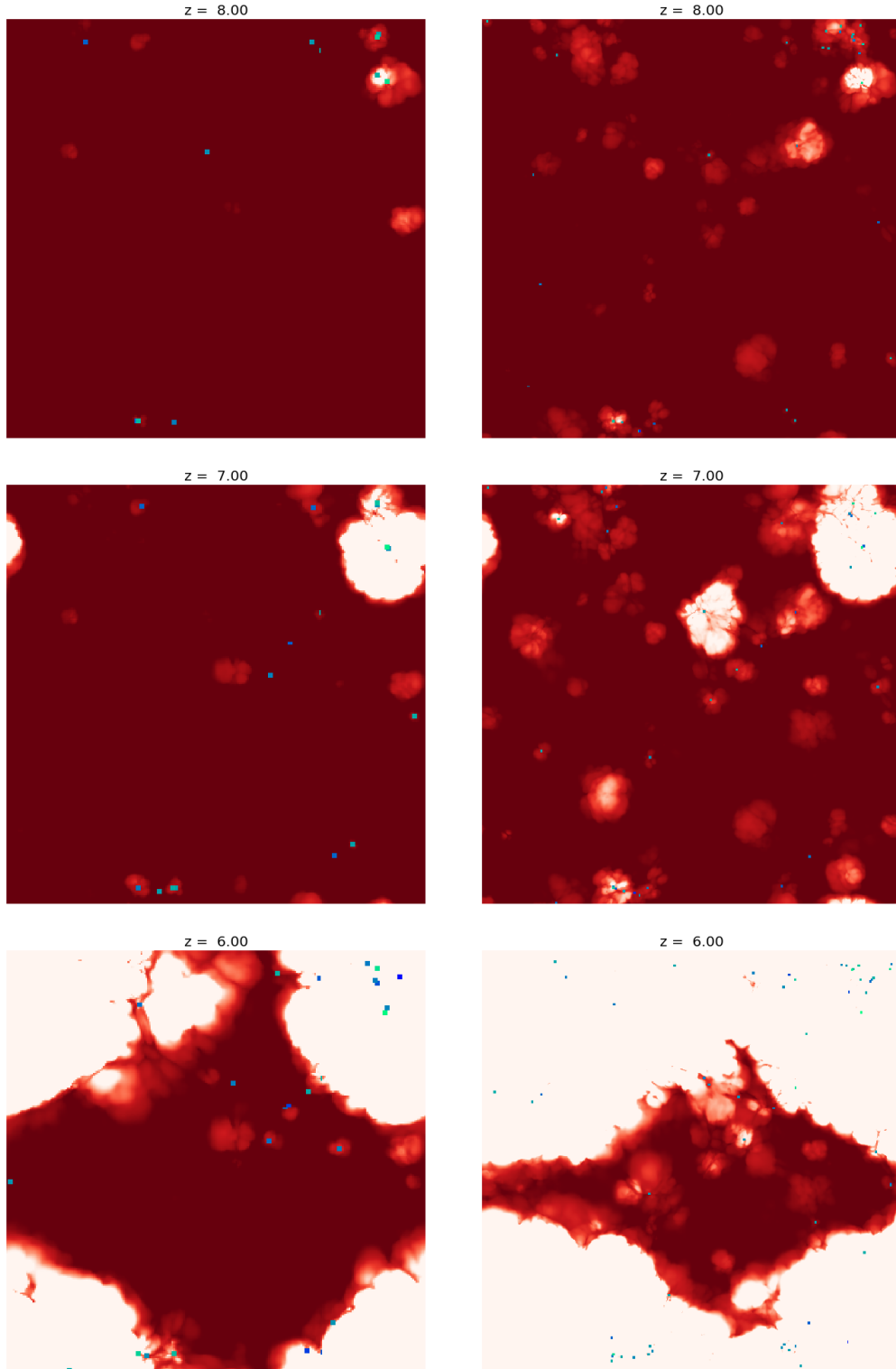


Figure 4. Projections of the logarithm of the neutral hydrogen fraction through the 6.4 Mpc volume at redshifts $z = 8, 7$ and 6 for the 256^3 (left column) and 512^3 (right column) test simulations. Note the increase in the number of relic HII regions in the high resolution simulation.

tion simulation, as compared to the lower resolution simulation. Many of these are relic HII regions as their sources have turned off according to our probabilistic model of star formation in low mass halos. One can also see that reionization has progressed further by $z = 6$ in the high resolution simulation, and that the strong ionization front driven by sustained star formation in the upper right corner of the cube is sweeping over smaller active and relic HII regions from earlier star formation in smaller halos. We explore this topic more thoroughly in the next section.

4.2. Science run—larger high-resolution volume

Here we present the results of the science run carried out at identical mass and spatial resolution to the 512_all run, but in a box 2.25 times the size. Because the volume is greater than $10\times$ that of the former, we have much better statistical coverage of the ionizing sources at all redshifts.

Fig. 5 shows how reionization proceeds through a series of projections of the HI fraction through the box. The color table is chosen to accentuate the small HII regions of low to moderate ionization fraction, while larger highly ionized HII bubbles appear white. Superimposed as blue and green pixels is the ionizing emissivity field. One sees that before the HMACHs begin to dominate the total ionizing budget at $z \sim 8$, the volume is filled with small HII regions which are only partially ionized. They increase in size and number, but are still largely isolated at $z = 9$. By this time, a cluster of higher mass galaxies forms in the upper right hand corner of the box, and their combined ionizing flux drives a strong ionization front into the IGM. Because of our small volume and periodic boundary conditions, this HII superbubble fills the entire volume by $z = 7.1$, sweeping over the smaller HII regions as well as a smaller superbubble percolating in the center of the box.

Fig. 6 shows the redshift evolution of the number of ionizing photons escaping from halos in various mass ranges. The MCs (red line) begin contributing at $z \sim 22$ and dominate the LMACHs (green line) at all redshifts down to $z \sim 6$. This is due to their higher numbers and escape fractions as compared to the LMACHs. In fact the MCs dominate the HMACHs (turquoise line) until $z \sim 10$, and become subdominant thereafter. The total ionizing photon flux is shown by the purple line, and increases by three orders of magnitude from $\dot{N} \sim 10^{49} \text{ s}^{-1} \text{ Mpc}^{-3}$ at $z = 17$ to $\dot{N} \sim 10^{52} \text{ s}^{-1} \text{ Mpc}^{-3}$ at $z = 7$, when overlap occurs.

The relative contribution of the different halo mass bins is illustrated in Fig. 7. As expected, MCs dominate the high redshift ionizing photon budget due to their high numbers and escape fractions. Interestingly, LMACHs are never more than a $\sim 20\%$ contributor, due to their significantly lower escape fractions. The HMACHs begin forming at $z \sim 16$ in this simulation, and only begin to exceed the contribution of the MCs at $z \sim 10$, and of MCs+LMACHs at $z \sim 9$. This figure makes it clear that the contribution of the MCs to the early phases of reionization $15 \geq z \geq 10$ cannot be ignored, and is more significant than that of the LMACHs.

Fig. 8 shows the evolution of the ionized volume fraction f_i for three levels of ionization fraction (So et al. 2014): 10%, 99.9%, and 99.999%. The left(right) panel shows the linear(log) of the ionized volume fraction, respectively. Looking at the left panel first, we see that low levels of ionization (10%) are obtained in larger fractions of the volume than high levels of ionization $\geq 99.9\%$ at all redshifts, but is more pronounced at high redshifts. As found by So et al. (2014), the curve for the highest level of ionization 99.999% is significantly

displaced to lower redshifts relative to the other two, and reaches $f_i = 1$ at $z = 6$, a $\Delta z = 1$ later.

Looking at the right panel, we see by the blue curve that lower levels of ionization begin to occupy tiny fractions of the volume before $z = 20$, consistent with the photon production history shown in Fig. 6. The blue curve increases monotonically to lower redshifts, reaching $f_i = 1$ at $z = 7.1$. The green curve shows the fraction of the volume that reaches the threshold of 99.9% local ionization fraction. It is not monotonic, but shows a sawtooth like modulation. This is a consequence of our insertion of a new set of ionizing sources every 20 Myr. While the periodicity is an artifact of our insertion method, some variability in f_i would be expected at early times in the continuous insertion limit as star formation in low mass halos turns on and off, creating relic HII regions in the process.

Fig. 9 depicts the state of affairs at $z = 10$, when HMACHs begin to dominate the photon budget. Fig. 9a is a projection of the ionizing emissivity field. We see the volume is filled with many hundreds of ionizing sources. The sources are clustered; one can see in Fig. 9b the sources trace the density field.

Figs. 9c and 9d show slices of HI fraction and temperature through the most massive halo in the box at $z = 10$. One sees a couple of larger HII regions with $T > 10^4 \text{ K}$ and $f_{\text{HI}} < 10^{-3}$ and numerous smaller HII regions of lower temperature and higher neutral fraction. The former mark the locations of HMACHs, which form stars continuously in our model, while the latter mark the locations of MCs and LMACHs, which form stars intermittently below $M_{\text{halo}} = 10^{8.5} M_{\odot}$, resulting in smaller, cooler, recombining HII regions.

5. DISCUSSION AND CONCLUSIONS

In this paper, we study the role of low mass halos in reionization. Using fully-coupled cosmological radiation hydrodynamic simulations with a subgrid model for the ionizing sources derived from the *Renaissance Simulations* (Xu et al. 2016b), we find that galaxies of dynamical mass $10^7 M_{\odot} < M_{\text{halo}} < 10^8 M_{\odot}$ make an important contribution to the earliest stages of reionization, in agreement with the findings of Wise et al. (2014). Halos in this mass range have been neglected in previous studies because they were assumed to form stars at negligible rates due to inefficient H_2 cooling. However Wise et al. (2014) showed that these so-called metal cooling halos (MCs) can cool by metal fine-structure lines and form stars if they have been enriched by ejecta from Pop III supernovae. Although the star formation efficiency is still quite low, this is compensated for by the MCs high space density and ionizing escape fraction. Interestingly, we find that MC's ionizing contribution dominates that of the LMACHs ($10^8 M_{\odot} < M_{\text{halo}} < 10^9 M_{\odot}$) over the entire redshift range before HMACHs ($M_{\text{halo}} > 10^9 M_{\odot}$) become the dominant ionizers at $z \approx 10$.

The main effect of including MCs into reionization models is that reionization starts earlier, boosting τ_{es} slightly. However the redshift of reionization completion (overlap) is only marginally affected. This reinforces but extends to lower mass halos the earlier findings of Iliiev et al. (2007), who examined the role of LMACHs on reionization. Referring to Table 2, comparing the two 6.4 Mpc box simulations with and without MCs, the difference in τ_{es} before overlap is about 0.0023, which is about a 5% increase. However, the dominant factor influencing the total optical depth is the redshift of overlap, which for our 14.4 Mpc box simulation is $z_{\text{ov}} = 7.08$. The contributions to τ_{es} before and after overlap are 0.0146 and

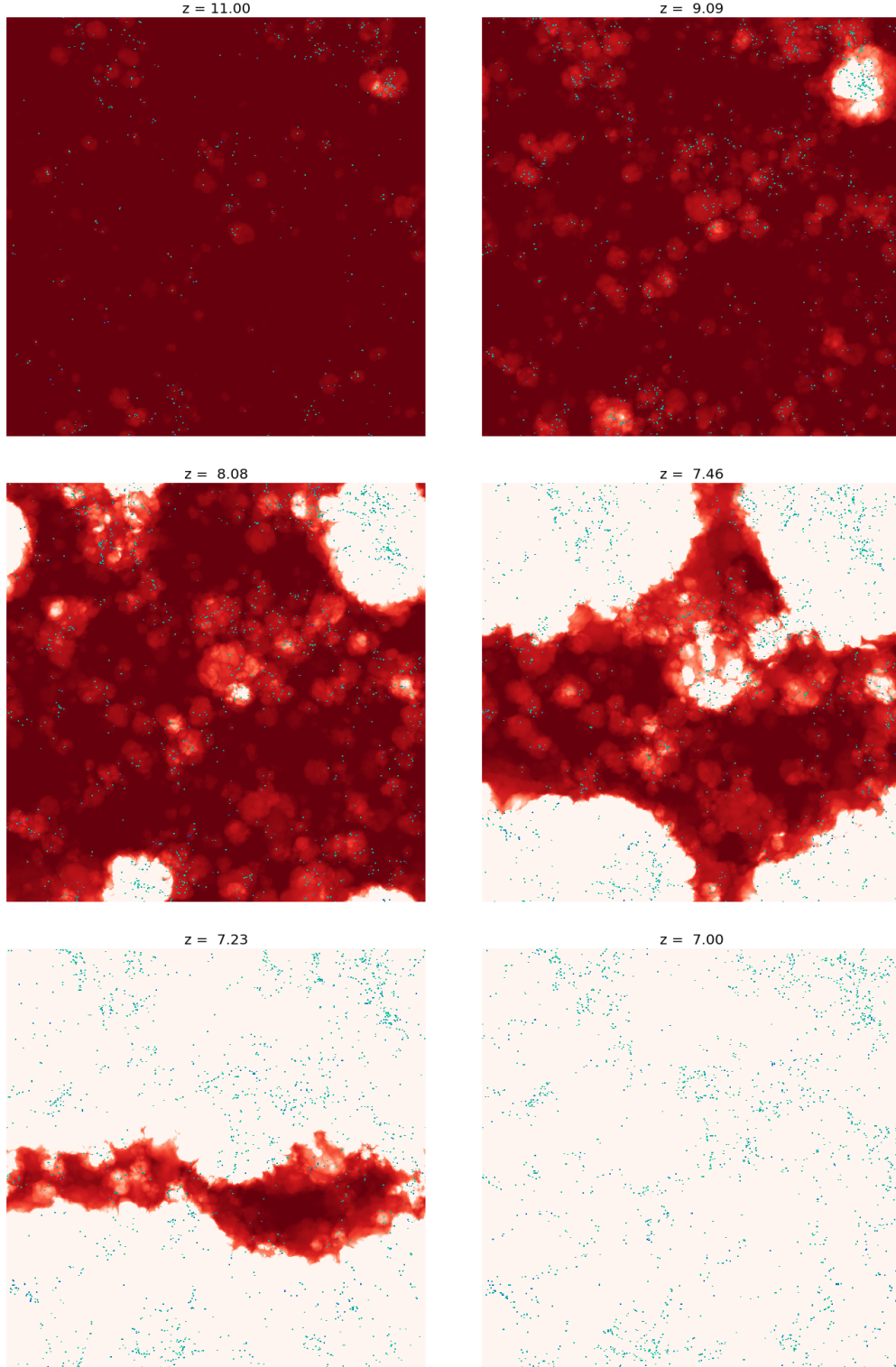


Figure 5. Projections of the logarithm of the neutral hydrogen fraction and ionizing emissivities (blue points) through the 14.4 Mpc volume at redshifts $z = 11, 9.09, 8.08, 7.46, 7.23$ and 7 . This 1152^3 simulation has identical mass and spatial resolution as the 512^3 test simulation, but ionizes considerably earlier.

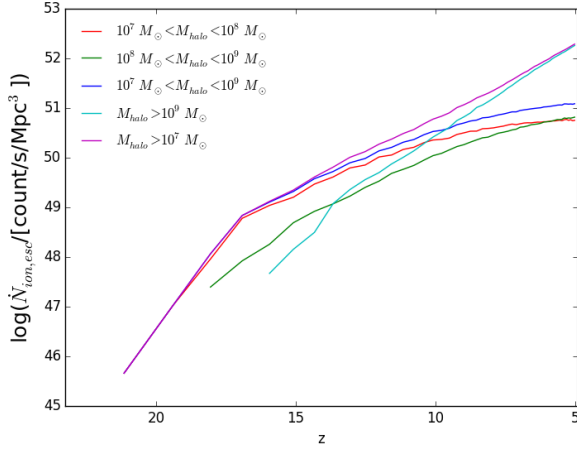


Figure 6. Number of escaping ionizing photons coming from halos in different mass bins from the 1152_all simulation. Blue line: $10^7 \leq M_{\text{halo}}/M_{\odot} \leq 10^8$; green line: $10^8 \leq M_{\text{halo}}/M_{\odot} \leq 10^9$; red line: $10^9 \leq M_{\text{halo}}/M_{\odot} \leq 10^{10}$; turquoise line: $M_{\text{halo}}/M_{\odot} > 10^{10}$. The purple line is the sum over all halos.

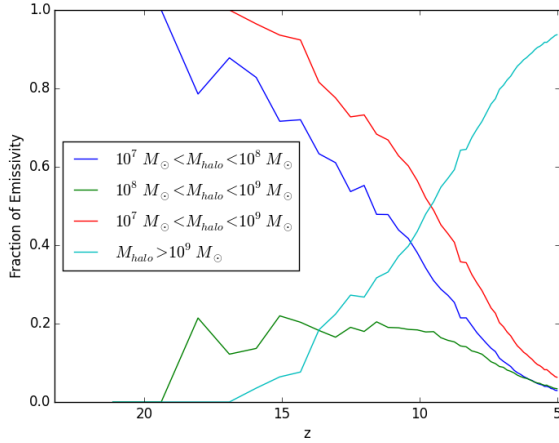


Figure 7. The fraction of the total ionizing luminosity coming from halos in different mass bins from the 1152_all simulation. Blue line: $10^7 \leq M_{\text{halo}}/M_{\odot} \leq 10^8$; green line: $10^8 \leq M_{\text{halo}}/M_{\odot} \leq 10^9$; red line: $10^9 \leq M_{\text{halo}}/M_{\odot} \leq 10^{10}$; and turquoise line: $M_{\text{halo}}/M_{\odot} > 10^{10}$.

0.0544, respectively, for a total of 0.0691, marginally consistent with the latest Planck satellite results (Planck Collaboration et al. 2016).

Our simulations suffer from several limitations, which we discuss here. The first is the omission of the contribution of Pop III stars to the ionizing photon budget. Pop III star formation is not included in our simulation, and therefore, the very first sources of ionizing photons are omitted entirely. Simulations that include this physics show that the Pop III SFR increases for the first 100 Myr, and then remains approximately constant at a level of $5 \times 10^{-5} M_{\odot} \text{ yr}^{-1} \text{ Mpc}^{-3}$ until overlap (Wise et al. 2012; Xu et al. 2016a). Assuming an ionizing photon to stellar baryon number ratio of 60,000 (Schaerer 2002), then this corresponds to a constant ionizing flux from Pop III stars of $1.1 \times 10^{50} \text{ s}^{-1} \text{ Mpc}^{-3}$. Referring to Fig. 6 we see that small galaxies begin to exceed this average emissivity at $z \approx 13$ and dominate it by 1.5 orders of magnitude by overlap. Wise et al. (2014) presented one-zone reionization models with and without Pop III stars, and found

that their inclusion boosted the ionized mass fraction by less than 10% at all redshifts $z < 20$, and increased z_{ov} by a small amount. We therefore conclude that the results presented here would not be qualitatively changed by the inclusion of Pop III stars.

The second limitation is the use of a non-evolving mapping from halo mass to escaping ionizing emissivity. As described previously, Table 1 is taken from an analysis of a $z = 12.5$ snapshot of the *Normal Renaissance Simulation*. Ideally, one would like to use a redshift-dependent set of tables that span the entire reionization history. One can ask how different might the results be if we had done that? To address this we rely on the extensive discussion of the evolution of the ionizing escape fraction in the *Renaissance Simulations* in Xu et al. (2016b), Sec. 4. They found that f_{esc} depends primarily on halo mass, and is rather insensitive to redshift or large-scale environment. This is illustrated in Figs. 18-20 of Xu et al. (2016b), which shows f_{esc} and $\dot{N}_{\text{ion,esc}}$ versus M_{halo} for several redshifts from each of the three simulations. The figures show that evolution of the ionizing photon budget comes almost entirely from the evolving halo population, and not from the $f_{\text{esc}}-M_{\text{halo}}$ relation which is remarkably constant with respect to redshift and environment. This is true for both the median as well as the scatter, which increases significantly below $10^8 M_{\odot}$. This is one input to our emissivity model. The other input is the probability that a halo of a given mass is actively forming stars at a given time. Xu et al. (2016b) show that this probability declines from unity at $M_{\text{halo}} \approx 10^{8.5} M_{\odot}$, is roughly 50% (10%) at $M_{\text{halo}} = 10^8 (10^7) M_{\odot}$, and zero below $M_{\text{halo}} \approx 10^{6.5} M_{\odot}$. However, for a given region these fractions decrease with time for halos below $10^8 M_{\odot}$ because of the increasing effects of radiative feedback from more massive galaxies which increase the filtering halo mass for efficient cooling and star formation. This effect is not included in our model. During the onset of reionization, HII regions are primarily isolated before the overlap phase, and these galaxies are regulated from their own radiative and supernova feedback, unaffected from radiation originating from other galaxies. Therefore, the results from the Renaissance Simulations provides a good estimate of the ionizing photon production from these early galaxies. Only afterwards does the filtering effect for MCs becomes important precisely when the HMACHs begin to dominate the ionizing budget at $z \approx 10$. Therefore our main conclusion that MCs make an important contribution to early reionization, but have minimal contribution to the late stages of reionization, is unaltered by omitting the effect of filtering.

A third limitation is that our simulation volume is not large enough to adequately represent the characteristics of reionization on the largest scales. Our requirement to include halos as small as $10^7 M_{\odot}$ dictated the choice of a small box size to keep the computational cost reasonable. According to Iliev et al. (2014), a comoving volume of $\sim 100 \text{ Mpc}/h$ per side is needed for simulating a convergent mean reionization history. We therefore cannot claim our z_{ov} is converged. Running a $100 \text{ Mpc}/h$ box while resolving $10^7 M_{\odot}$ halos is not feasible on current supercomputers. However one could adopt the approach of Ahn et al. (2012), who incorporated the contribution of Pop III ionizing sources in a large scale reionization simulation via a subgrid model derived from a small box simulation. The approach would carry over to the case of MCs, with some modifications needed to take into account the stochastic nature of star formation in such halos.

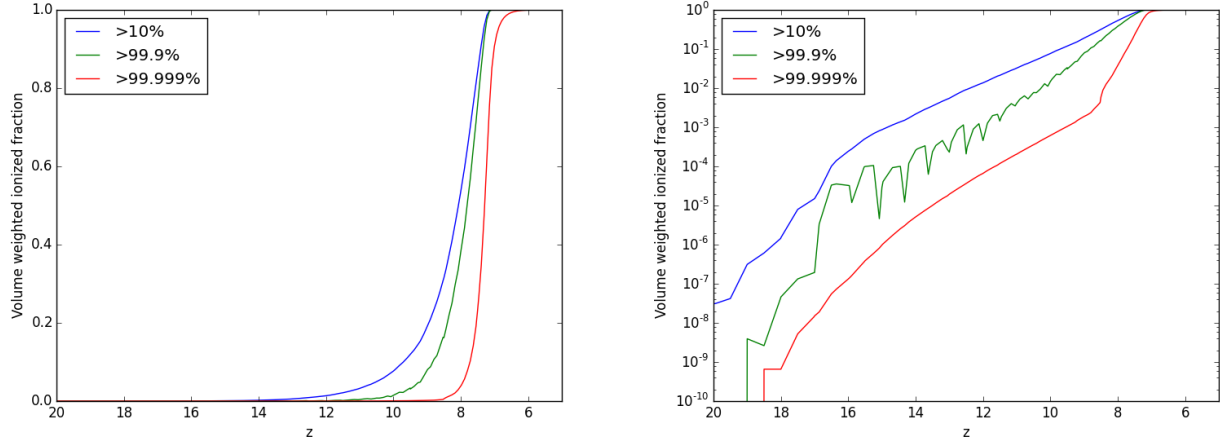


Figure 8. Ionized volume fraction versus redshift for different ionization fraction thresholds. Top: linear scale, Bottom: logarithmic scale. Relic HII regions show up prominently in the 99.9% curve as sources are reintroduced on 20 Myr intervals.

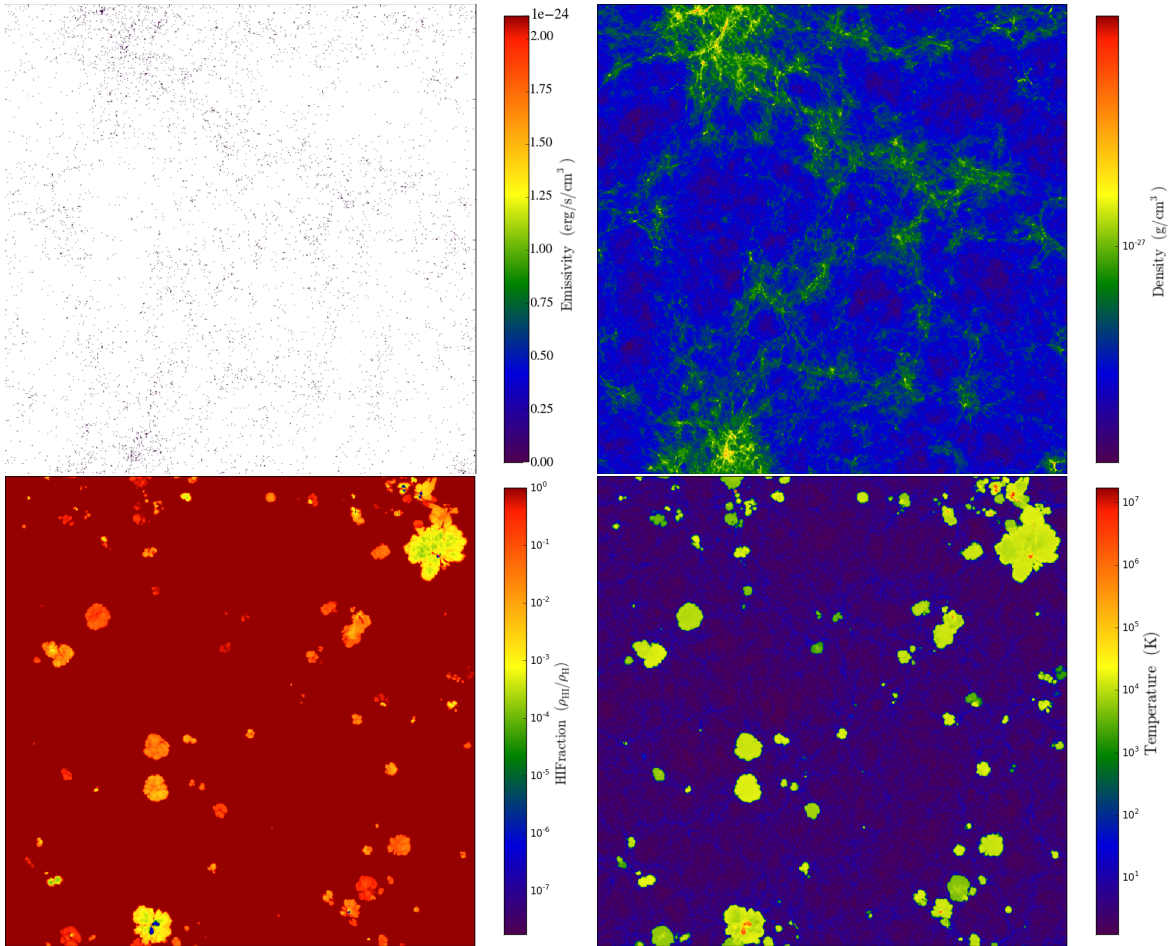


Figure 9. State of the IGM at $z=10$, when HMACHs ($M_{\text{halo}} > 10^9 M_{\odot}$) begin to dominate the ionizing photon budget. Top: projections of the ionizing emissivity field (left) and logarithm of the baryon density (right) through the 14.4 Mpc volume. Bottom: thin slices of the HI fraction (left) and gas temperature (right) fields at the same redshift.

5.1. Comparable Works

5.1.1. Ocvirk et al. (2016)

Ocvirk et al. (2016) study the reionization history of the Local Group using the radiation hydrodynamic cosmology code RAMSES-CUDATON. Star formation and radiative feedback is modeled inline with the simulation using a simple parameterized model on a uniform Cartesian grid of size 91 comoving Mpc on a side, resolved by 4096^3 cells and the same number of particles. The spatial and dark matter mass resolution is approximately 2 times and 6 times poorer than our 1152^3 simulation, and does not include halos in the mass range $10^7 \leq M/M_\odot \leq 10^8$, which is the focus of our investigation. Because galaxies are not resolved in their simulation, a uniform ionizing escape fraction $f_{\text{esc}} = 0.5$ is assumed. This simulation has an overlap redshift of $z_{\text{ov}} = 4.6$ because of their low star formation efficiencies, and they correct their analysis by a redshift contraction factor in post-processing. By contrast, we import the results of high resolution galaxy formation simulations into our reionization model, which include details of the halo mass dependence of the escape fraction and the bursty nature of star formation. The approaches are significantly different, independent of box size.

5.1.2. Kimm et al. (2017)

As this manuscript was being finalized for submission, a new paper appeared which directly addresses the same question we are exploring: the role of the smallest galaxies to reionization. Kimm et al. (2017) perform AMR simulations of high redshift galaxies very similar in design and objectives as Wise et al. (2014) and found very similar results. Specifically, they used the RAMSES-RT code (Rosdahl & Teyssier 2015) to simulate the assembly of the first galaxies in a 2 comoving Mpc box including the feedback by Pop III stars forming in minihalos. Importantly, they cover the halo mass range $10^7 \leq M/M_\odot \leq 10^8$, albeit with far smaller samples than Xu et al. (2016b). While the numerical methods differ from those employed by Wise et al. (2014) and Xu et al. (2016b), the physical ingredients are essentially the same, including details of the star formation and feedback models. Their results can thus be compared directly.

Kimm et al. (2017) find that the mean ionizing escape fraction increases with decreasing halo mass, in agreement with (Wise et al. 2014; Xu et al. 2016b), although they quote a slightly lower range of 20-40% for the smallest halos. They find that star formation in individual halos is very stochastic, with recovery times from stellar feedback ranging from ~ 20 to 200 Myr. They do not compute a halo occupation fraction of active star formation versus halo mass as done by Xu et al. (2016b). However the M_{star} vs. M_{halo} data shown in their Fig. 5 is in good agreement with Xu et al. (2016b)'s results for $M_{\text{halo}} > 10^7 M_\odot$, but displays somewhat lower stellar masses for smaller halos.

Kimm et al. (2017) do not perform an inhomogeneous reionization simulation as we do, but they do present a one-zone model using their results and those from Kimm & Cen (2014) as input from which they derive conclusions about the importance of minihalos ($M_{\text{halo}} < 10^8 M_\odot$) to reionization. Here we compare our conclusions and highlight points of agreement and difference. We agree that minihalos dominate the earliest stages of reionization and that HMACHs dominate the late stages of reionization leading to overlap. The redshift at which the HMACHs become dominant is similar in both models: $z \approx 11$ in Kimm et al. (2017) and $z \approx 10$ in this work.

Where we differ is the relative contribution of LMACHs and minihalos (which includes what we are calling MCs). Kimm et al. (2017) find that LMACHs begin to dominate minihalos at $z \approx 17$ (see their Fig. 15), whereas we find they are subdominant at all redshifts prior to overlap (Fig. 7). For the purposes of their one zone reionization model, Kimm et al. (2017) assume in their fiducial model escape fractions of about 10-20% for LMACHs, whereas Xu et al. (2016b) measures values of a few percent across that mass range. Kimm et al. (2017) also consider a "Low" model which adopts low values of f_{esc} for LMACHs, consistent with Xu et al. (2016b). But the Low model has a constantly declining f_{esc} as a function of M_{halo} , which severely underpredicts f_{esc} for HMACHs when compared to both of our simulations. This model reionizes late and underpredicts τ_{es} by a considerable factor. Our model reionizes at $z \approx 7$ and is in reasonable agreement with the observed τ_{es} . We therefore disagree with Kimm et al. (2017)'s conclusion that minihalos are unimportant for reionization, a conclusion that rests on the differences between the f_{esc} values of the LMACHs of our comparable works. However, we do agree with their conclusion that halos as small as $10^8 M_\odot$ must be included in reionization simulations, and this discussion only highlights the need to understand their properties better through more comprehensive simulations.

This research was supported by National Science Foundation (NSF) grants AST-1109243 and to M.L.N. J.H.W. acknowledges support from NSF grants AST-1614333 and AST-1333360 and Hubble Theory grants HST-AR-13895 and HST-AR-14326. The simulations were performed using the ENZO code on the Comet system at the San Diego Supercomputer Center, University of California San Diego with support from XRAC allocation MCA-TG98020N to M.L.N. This research has made use of NASA's Astrophysics Data System Bibliographic Services. The majority of the analysis and plots were done with YT (Turk et al. 2011). ENZO and YT are developed by a large number of independent researchers from numerous institutions around the world. Their commitment to open science has helped make this work possible.

REFERENCES

- Ahn, K., Iliev, I. T., Shapiro, P. R., et al. 2012, *ApJ*, 756, L16
- Anninos, P., Zhang, Y., Abel, T., & Norman, M. L. 1997, *New Astronomy*, 2, 209
- Bryan, G. L., Norman, M. L., Stone, J. M., Cen, R., & Ostriker, J. P. 1995, *Computer Physics Communications*, 89, 149
- Bryan, G. L., Norman, M. L., O'Shea, B. W., et al. 2014, *ApJS*, 211, 19
- Choudhury, T. R., Ferrara, A., & Gallerani, S. 2008, *MNRAS*, 385, L58
- Hockney, R. W., & Eastwood, J. W. 1988, *Computer simulation using particles*
- Iliev, I. T., Mellema, G., Ahn, K., et al. 2014, *MNRAS*, 439, 725
- Iliev, I. T., Mellema, G., Shapiro, P. R., & Pen, U. 2007, *MNRAS*, 376, 534
- Iliev, I. T., Mellema, G., Shapiro, P. R., et al. 2012, *MNRAS*, 423, 2222
- Kimm, T., & Cen, R. 2014, *ApJ*, 788, 121
- Kimm, T., Katz, H., Haehnelt, M., et al. 2017, *MNRAS*, arXiv:1608.04762
- Norman, M. L., Reynolds, D. R., So, G. C., Harkness, R. P., & Wise, J. H. 2015, *ApJS*, 216, 16
- Ocvirk, P., Gillet, N., Shapiro, P. R., et al. 2016, *MNRAS*, 463, 1462
- O'Shea, B. W., Wise, J. H., Xu, H., & Norman, M. L. 2015, *ApJ*, 807, L12
- Planck Collaboration, Adam, R., Aghanim, N., et al. 2016, *A&A*, 596, A108
- Reynolds, D. R., Hayes, J. C., Paschos, P., & Norman, M. L. 2009, *Journal of Computational Physics*, 228, 6833
- Ricotti, M., Gnedin, N. Y., & Shull, J. M. 2002, *ApJ*, 575, 49
- Rosdahl, J., & Teyssier, R. 2015, *MNRAS*, 449, 4380
- Schaerer, D. 2002, *A&A*, 382, 28
- Shapiro, P. R., Iliev, I. T., Mellema, G., et al. 2012, in *American Institute of Physics Conference Series*, Vol. 1480, American Institute of Physics
- Skory, S., Turk, M. J., Norman, M. L., & Coil, A. L. 2010, *ApJS*, 191, 43
- So, G. C., Norman, M. L., Reynolds, D. R., & Wise, J. H. 2014, *ApJ*, 789, 149

- Turk, M. J., Smith, B. D., Oishi, J. S., et al. 2011, *ApJS*, 192, 9
- Wise, J. H., & Abel, T. 2011, *MNRAS*, 414, 3458
- Wise, J. H., Demchenko, V. G., Halicek, M. T., et al. 2014, *MNRAS*, 442, 2560
- Wise, J. H., Turk, M. J., Norman, M. L., & Abel, T. 2012, *ApJ*, 745, 50
- Wyithe, J. S. B., & Loeb, A. 2013, *MNRAS*, 428, 2741
- Xu, H., Norman, M. L., O'Shea, B. W., & Wise, J. H. 2016a, *ApJ*, 823, 140
- Xu, H., Wise, J. H., Norman, M. L., Ahn, K., & O'Shea, B. W. 2016b, *ApJ*, 833, 84